Compact Multilayer Bandpass Filter Using Low-Temperature Additively Manufacturing Solution

Mengze Li, Student Member, IEEE, Yang Yang, Senior Member, IEEE, Francesca Iacopi, Senior Member, IEEE, Minoru Yamada, Jaim Nulman, Senior Member, IEEE

***Abstract*—This paper presented an additively manufactured bandpass filter (BPF) based on a second-order stub-loaded resonator consisting of multi-metal layer components. The proposed BPF is fabricated by a low-temperature (140℃) additively manufactured electronics (AME) solution that can fabricate conductive and dielectric materials simultaneously with multi-metal-layer and flexible interlayer distance. By reducing the interlayer distance, constant inductance and capacitance can be realized in smaller sizes, which helps to achieve device minimization. Taking advantage of this inkjet printing technology, a second-order multi-metal layer resonator is proposed. To understand the principle of the BPF, an equivalent circuit with odd- and even-mode analysis is demonstrated. For verification, the frequency response of the circuit's mathematical model is calculated to compare with the electromagnetic simulation results. Good agreement can be achieved among the calculated, simulated, and measured results. The proposed BPF is designed at 12.25 GHz with a bandwidth of 40.8% and a compact size of 2.7 mm × 1.425 mm × 0.585 mm or 0.186λg × 0.098λg× 0.040λg, which is suitable for circuit-in-package applications in television programs, radar detection and satellite communications.**

***Index Terms*—bandpass filter (BPF), wide stopband, multi-metal-layer components, additively manufactured electronics (AME), low-temperature, 3D inkjet printing.**

I. Introduction

With the rapid development of additive manufacturing technology, more and more multi-material 3D printers can fabricate conductive and dielectric materials simultaneously, which have demonstrated their capabilities in electronic devices integration and 3D packaging [1]-[5]. However, it is still a challenge for these 3D printers to fabricate seamless multi-metal-layer in a single substrate. According to the open literature, multi-metal-layer technologies have an outstanding advantage in device minimization such as low-temperature co-fired ceramic (LTCC) [6]-[10] or semiconductor technologies [11]-[13]. For example, reference [8] proposes a compact LTCC diplexer with high-isolation. In [11], an on-chip miniaturized BPF is presented, which is based on a grounded center-tapped ring resonator with shunt capacitive loading. Although both designs demonstrated device minimization, these technologies are expensive and require complicated fabrication processes and longer production time. As an emerging technology, low-temperature additively manufacturing technologies have been applied in integrated electronic devices and packaging, such as electronic components [14], antenna arrays [15], terahertz lens [16], redistribution layers [17], combiner [18], transistors [19], and enzymatic biofuel [20].

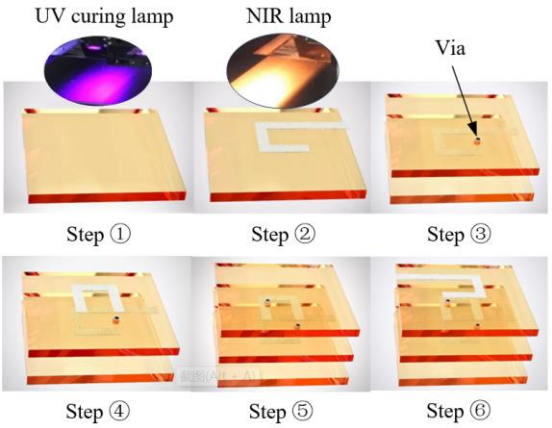

Fig. 1. The proposed low-temperature additively manufacturing electronics (AME) process.

In this paper, a low-temperature additively manufactured electronics (AME) solution is introduced for bandpass filter (BPF) design, taking advantage of dual-materials (conductive and dielectric materials) printing, as shown in Fig. 1. Nano Dimension's DragonFly LDM system is used for AME designs with 4pL printer heads. This system simultaneously jets both dielectric and conductive inks, hence simultaneously creating multilayer conductive structures within a single dielectric substrate. Compared with LTCC and semiconductor technologies, the AME solution is flexible on electronic device fabrication with design freedom adjusting the interlayer

This work was supported by Nano Dimension under a PhD scholarship agreement and UTS FEIT Blue Sky Grant. (Corresponding author:Yang Yang- yang.yang.au@ieee.org; yang.yang-1@uts.edu.au).

M. Li and Y. Yang are with the School of Electrical and Data Engineering, University of Technology Sydney, NSW, 2007, Australia.

Francesca Iacopi is with Australian Research Council Centre of Excellence in Transformative Meta-Optical Systems, School of Electrical and Data Engineering, University of Technology Sydney, NSW 2007, Australia.

Minoru Yamada and Jaim Nulman are with Nano Dimension, Science Park, Ness-Ziona, 7403635, Israel, and at 13798 NW 4th St, Suite 315, Sunrise, FL 33325, USA.

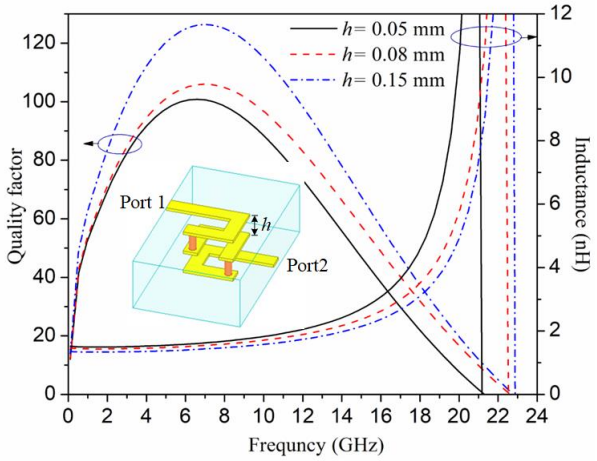

Fig. 2 Simulated inductances and quality factors of multilayer spiral inductors with different dielectric-layer thickness *h*.

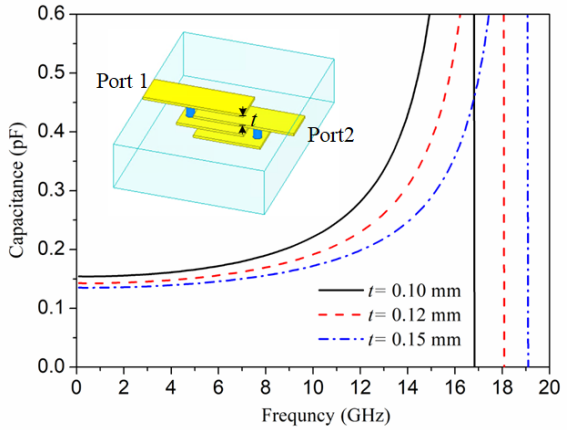

Fig. 3 Comparison of simulated capacitances of multilayer capacitors with different dielectric-layer thickness *t*.

distance. The printing process is carried out at a typical temperature of 140°C in a standard ambient atmosphere. For proof-of-concept, a multilayer BPF with vertically integrated capacitors and inductors has been designed, analyzed, fabricated and measured. Finite element electromagnetic field simulation analysis software, ANSYS High-Frequency Structure Simulator (HFSS), is used in the simulation, and the Vector Network Analyzer (VNA) used in the measurement is a Keysight PNA N5225B.

II. Additively Manufactured Components for Bandpass Filter Miniaturisation

The printed BPF is composed of the inductance and capacitance components. The proposed AME technique has the advantage of circuit miniaturization, which is demonstrated by using an inductor and a capacitor, as the examples.

A. Miniaturized 3D spiral inductor using AME process.

As shown in Fig. 1, the fabrication procedure of a 3D spiral inductor is demonstrated using the proposed low-temperature AME process. Silver nanoparticles and acrylate inks can be printed simultaneously in this AME process. During the manufacturing process, for *Step 1*, an ultraviolet (UV) lamp with a wavelength of 395 nm is used for curing the acrylate inks after they are ejected out from the nozzles. In *Step 2*, a metal strip line is printed on the acrylate layer. A near-infrared radiation (NIR) lamp with a wavelength of 0.75-1.4 μm and 140°C to 170°C process temperature is used to sinter the conductive inks. In *Steps 3 – 6,* acrylate and conductive inks are printed layer by layer to construct the 3D spiral inductor. Vias can be printed simultaneously in the acrylate layer to connect metal strip lines in different layers, as depicted in *Step 3*. Where a via is desired, no dielectric ink is deposited. This via can remain a through via hole or can be filled with the conductive silver nanoparticle ink. The fabrication is done layer by layer. Hence the silver is in the area where the filled via is being built, and the dielectric is around it. Taking advantage of the AME solution, designing 3D components and devices would be flexible.

For vertical spiral inductors, the inductance can be calculated by

$$L = K\frac{\mu_0\mu_r N^2 A_e}{H} \quad (1)$$

where μ_0 is the permeability of free space, μ_r is the relative permeability of the material, N is the total number of turns; H is the total height of coil, A_e is the section area of the coil, and K is a coefficient that depends on the ratio of r (radius of the coil) to H. To investigate the relationship between the L and H, Fig. 2 demonstrates the comparison of simulated inductances with different dielectric-layer thickness h. When h drops from 0.15 mm to 0.05 mm, the inductance increases gradually. In addition, Fig. 2 shows the quality factor versus different values of h. With the decline of h, the inductance density increases, which means that a higher inductance value can be obtained with a lower profile and constant plane size. A drop in peak quality factor is observed because increasing inductance usually involves increasing magnetic layer thickness, which leads to higher eddy currents.

B. Miniaturized capacitors with reduced interlayer distance

According to reference [21], for a multilayer capacitor, the capacitance "C" is given in the equation below:

$$c = \frac{\varepsilon_0\varepsilon_s S(n-1)}{t} \quad (2)$$

where ε_0 is the dielectric constant of free space, ε_s is the relative dielectric constant of the material, S is the effective area of the inner electrode. n is the number of inner electrodes, and t is the thickness of the dielectric layer.

Obviously, with the increase of the number of inner electrodes or raising the inner electrode effective area, the capacitance will grow. That is also the most common method to design a capacitor in previous literature. However, in this paper, the effect of the thickness of the dielectric layer are discussed. As shown in Fig. 3, with the decrease of dielectric-layer thickness t from 0.15mm to 0.10mm, capacitance increases significantly while the capacitor size keeps unchanged, consistent with equation (2). In other words, the adjustable interlayer distance can contribute to a smaller plane size and lower profile.

III. Multilayer BPF and Its Equivalent Circuit

A. Bandpass filter configuration

In Fig. 4(a), the 3-D view of the proposed BPF is presented.

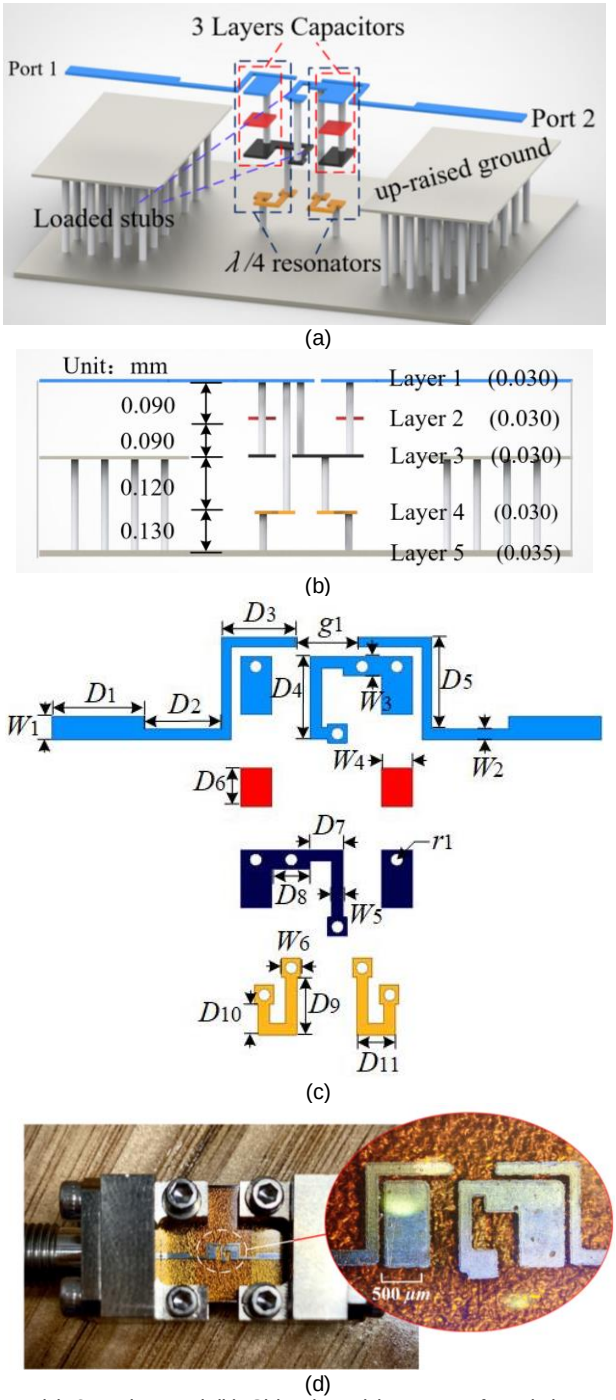

Fig. 4 (a) 3-D view and (b) Side view, (c) Layout of each layer, (d) Photograph of the 3D printed BPF with testing accessories and structural details of the filter under microscope.

Taking advantage of the proposed AME solution, the number of metal layers and the dielectric layer thickness among metal layers can be flexibly defined for circuit design. In this work, as shown in Fig. 4(b), five metal layers are employed to design the BPF, where layer 5 is used as the ground. The constructions of feeding lines and resonators are distributed from layer 1 to layer 4. The resonant part of the BPF consists of two λ/4 resonators, where three metal layers are stacked to form a compact capacitor. Two stepped-impedance stubs, located on layer 1 and layer 3, respectively, are loaded at the one third point to improve the of out-of-band suppression. Two up-raised grounds located at layer 3 are connected to the RF ground by 24 vias, respectively, to adjust the impedance match. Fig. 4(c) depicts the layout of the metal layers. Parameters of the proposed BPF are determined as follows (all in mm): D_1=3.3, D_2=1.6, D_3=1.28, D_4=1.3, D_5=1.305, D_6=0.85, D_7=0.4, D_8=0.5, D_9=0.85, D_{10}=0.425, D_{11}=0.7, W_1=0.5, W_2=0.125, W_3=0.4, W_4=0.65, W_5=0.15, W_6=0.4, r_1=0.1, g_1=0.7. The dimension of BPF excluding feeding lines is 2.7 mm × 1.425 mm × 0.585 mm or 0.186 λg × 0.098 λg× 0.040 λg, where λg is the guided wavelength at the center frequency. Fig. 4(d) shows the photograph of an additively manufactured prototype with testing accessories and structural details of the filter under a microscope.

B. Equivalent lumped component circuit

To facilitate the analysis of the proposed multi-metal layers BPF, an equivalent circuit based on the unfolded layout of the BPF is presented and discussed. Fig. 5 presents the equivalent lumped component (*LC*)-circuit model of the presented EM structure, where inductors and capacitors represent the high-impedance lines and the capacitive couplings, respectively. L_{Fi} (i=1, 2) denotes the self-inductances of the feeding lines. C_F is the capacitive coupling between the soldering area of SMK connector and the ground. C_b represents the coupling capacitance between the feeding line and the resonator. C_p is the bypass capacitance of the feeding line to the ground. In addition, the source to load coupling is modeled by $C_{S\text{-}L}$. The inductors and capacitors of the resonators are L_1 and C_1, where L_1 and C_1 represent the parasitic inductor and the capacitance of this three-dimension interdigital capacitor, respectively. L_2 is the self-inductance of the quarter wavelength resonator. The loaded stepped-impedance is represented by C_2, L_3 and C_3, L_4. C_2. L_3 denotes the low-impedance segment. The C_3 and L_4 denote the high-impedance segment.

C. Analysis of equivalent LC-circuit model

For circuit analysis, an equivalent *LC*-circuit of resonators is depicted in Fig. 6(a). Since the two resonators are symmetrical about AA′, odd- and even-mode circuits can be obtained, as shown in Figs. 6(b) and (c). The loop equation method is used for circuit analysis, of which the loop currents I_i (i=1, 2, 3, 4) are marked in Figs. 6(b) and (c). The expressions of input admittance are listed to calculate the resonant frequencies of transmission poles (TPs) and transmission zeros (TZs).

Applying Kirchhoff's voltage law (KVL) to the odd-mode equivalent circuit in Fig. 6(b), the voltage equations of the four loops are expressed as:

$$\frac{I_1}{sC_1}+sL_1I_1+sL_2(I_1-I_2)-U_{odd}=0 \tag{3}$$

$$\frac{(I_2-I_3)}{sC_2}+sL_2(I_2-I_1)=0 \tag{4}$$

$$\frac{(I_3-I_2)}{sC_2}+sL_3I_3+\frac{(I_3-I_4)}{sC_3}=0 \tag{5}$$

$$sL_4I_4+\frac{(I_4-I_3)}{sC_3}=0 \tag{6}$$

Similarity, applying KVL to the even-mode equivalent circuit in Fig. 6(c), the voltage equations of the three loops are

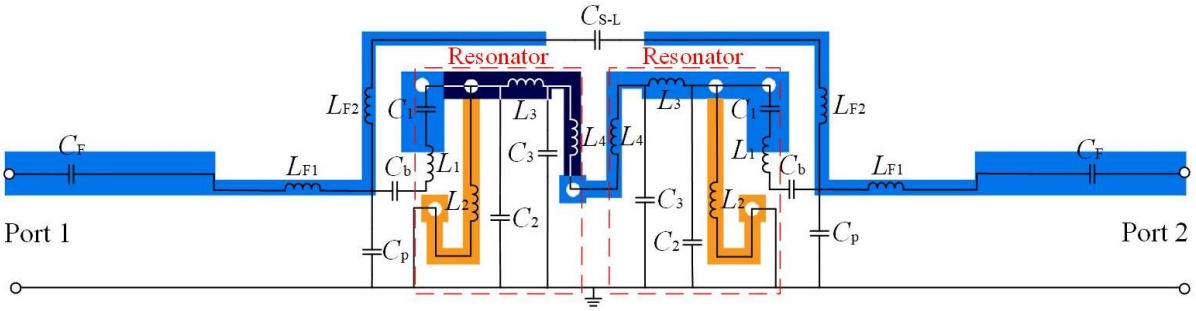

Fig. 5 Equivalent *LC*-circuit model based on unfolded layout of the proposed BPF (Derived from Fig. 4(a) for illustration of the LC components).

expressed as:

$$\frac{I_1}{sC_1}+sL_1I_1+sL_2(I_1-I_2)-U_{even}=0 \tag{7}$$

$$\frac{(I_2-I_3)}{sC_2}+sL_2(I_2-I_1)=0 \tag{8}$$

$$\frac{(I_3-I_2)}{sC_2}+sL_3I_3+\frac{I_3}{sC_3}=0 \tag{9}$$

where U_{odd} and U_{even} denote the input voltages of odd- and even- mode circuits, respectively. s is a complex variable in proportion to angular frequency ω. Therefore, the relationships between input voltages and input admittances in Figs. 6(b) and (c) can be written as:

$$Y_{odd}(s)=\frac{I_{1\_odd}(s)}{U_{odd}(s)}=\frac{I_{1\_odd}(j\omega_{odd})}{U_{odd}(j\omega_{odd})} \tag{10}$$

$$Y_{even}(s)=\frac{I_{1\_even}(s)}{U_{even}(s)}=\frac{I_{1\_even}(j\omega_{even})}{U_{even}(j\omega_{even})} \tag{11}$$

where ω denotes angular frequency, and j is a pure imaginary unit number. Using MATLAB, the expression of input admittances consists of complex variable s and lumped LC-elements can be deduced by solving equations (2)-(11). Since $\omega=2\pi f$, the frequencies f_{odd} and f_{even} (corresponding to odd- and even-mode) can be calculated when $Y_{odd}(j\omega)=0$ and $Y_{even}(j\omega)=0$, respectively. Meanwhile, the TZs can be determined when $Y_{odd}(j\omega)=Y_{even}(j\omega)$. For verification, the equivalent LC-circuit is optimized to match the finite element electromagnetic field simulation result of the EM structure. As shown in Fig. 7(a), the simulated results of equivalent LC-circuit carried by ADS are illustrated. Good agreement can be obtained between the calculated results of LC-circuit and simulated results of the EM structure. Substituting the obtained values of lumped elements in equivalent circuit: L_1= 0.016 nH, L_2=0.589 nH, L_3=0.725 nH, L_4=1.247 nH, C_1=0.345 pF, C_2=0.18 pF, C_3=0.11 pF into equations (12)-(13), one TZs f_{zi} (i=1) and two TPs f_{pi} (i=1,2) can be obtained in the frequency range of 0-35 GHz through the calculations. Finally, the estimated TZs and TPs are marked at Fig. 7(a) as well. Compared with the simulated results of TZs and TPs: f_{z1} =19.85 GHz, f_{p1} =11.31 GHz and f_{p2} =13.18 GHz, the calculated results agree well with the simulated ones. In addition, to improve the skirt selectivity, (source-load) S-L coupling is induced by adding a capacitor between two ports, as shown in Fig. 7(b). The locations of the TZs are dependent on the mixed electromagnetic (EM) coupling coefficient between the two resonators and the (source-load) S-L coupling construction. Since these two resonators of the BPF are

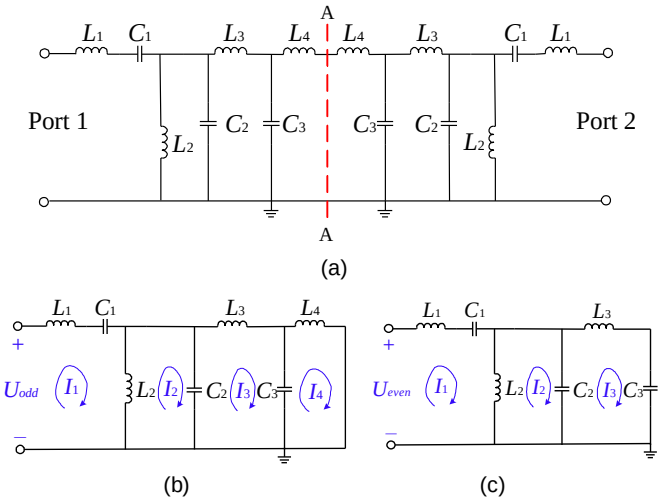

Fig. 6 (a) Equivalent circuit of the resonators and its (b) Odd- and (c) Even-mode equivalent circuits.

connected by via, which results that the magnetic coupling is larger than the electric one. Therefore, a TZ would be excited at the upper (magnetic-dominant coupling) stopband (TZ_2). As shown in Fig. 8(a), the frequency response of the coupled resonators against spacing D_7 is depicted, which shows the variation of the EM coupling between the two resonators. Lower-band TZ (TZ_1) and upper-band TZ (TZ_2) are marked in the picture. By tuning D_7, the location of the TZ_2 can be adjusted at the upper stopband, which significantly enhances the out-of-band attenuation of the proposed filter, while the TZ_1 keeps unchanged.

In addition, the simulated frequency response against g_1 is given for the TZ created in the low-band (TZ_1), as shown in Fig. 8(b). When g_1 decreases from 0.3 to 0.1 mm, the TZ_1 increases from 5.88 to 8.37 GHz, whereas the TZ_2 changes slightly without affecting the filter bandwidth. The closer the TZs to the passband, the better the frequency selectivity can be achieved.

For the frequency response of the TPs, by solving $Y_{odd}(j\omega)=0$ and $Y_{even}(j\omega)=0$, it can be found that the even-mode resonant frequency f_{even} is the function of L_4, while f_{odd} is the function of both L_2 and L_4. L_2 and L_4 correspond to the length of D_4 and D_{10} in the EM structure, respectively. For validation, the simulated responses against D_4 and D_{10} are shown in Figs. 8(c) and (d). When D_4 rises from 0.9 mm to 1.3 mm, f_{p1} keeps constant while f_{p2} decreases gradually. Besides, with the development of D_{10}, f_{p1} and f_{p2} decline simultaneously. The variations are consistent with the analysis and verify that the bandwidth and center frequency can be flexibly designed.

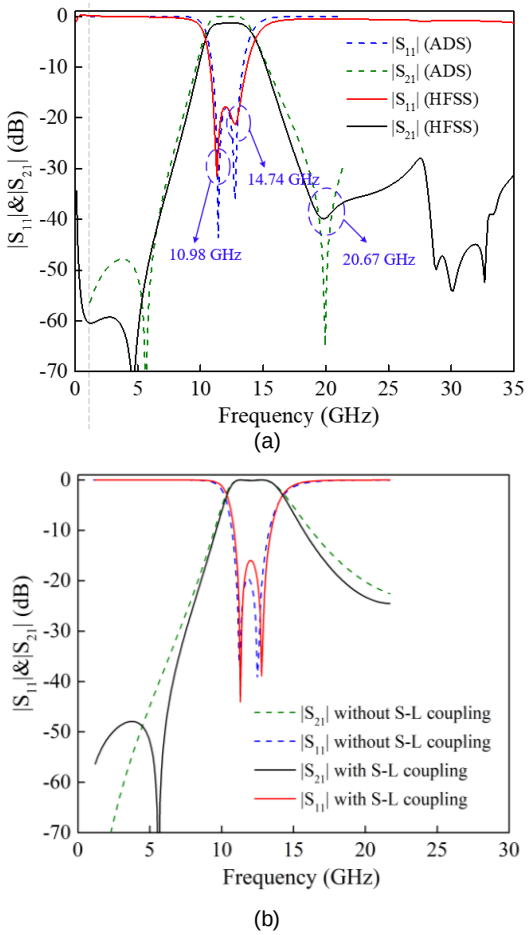

Fig. 7 Simulated frequency responses of (a) the BPF (by HFSS) as well as the equivalent *LC*-circuit in Fig. 6 (by ADS) and (b) Simulated frequency responses of the BPF with or without S-L coupling.

The unloaded quality factor of the resonators is important for filter performance. In Fig. 9(a), for a single resonator used in the proposed BPF (center frequency = 12.25 GHz), the simulated unloaded Q-factor versus the length $L=D_9+D_{10}+D_{11}$ is presented. According to Fig.9(a), when L increases, the unloaded Q_u decreases due to dielectric and conductor losses. Besides, the external quality factor Q_e with varied coupling gap G is depicted in Fig. R2 (b). When G increases from 0.05 to 0.5mm, a higher Q_e of the filter can be obtained, which causes a decrease of the bandwidth.

D. Suppression of third harmonic and wide stopband

Fig. 10(a) shows the structure of the quarter-wavelength resonator used in the proposed BPF. A short-circuited stepped impedance stub is loaded at the trisection-point of this resonator closing to the input terminal. The electrical lengths of the quarter-wavelength transmission line are referred to θ_1 and $2\theta_1$, respectively. The short-circuited stub position can be defined by analyzing the voltage distributions of the fundamental mode and the third harmonic to improve the out-of-band suppression. It is obvious that the shorted terminal of the quarter-wavelength resonator is the common voltage zero point of the fundamental mode and the third harmonic mode, while the trisection-points near the input terminal is the zero-voltage point only for third harmonic modes. When the shorted stub is located at the zero-voltage point of the third harmonic mode, the third harmonic mode signal will not get through the resonator, as shown in Fig. 10(b). Thus, out-of-band suppression can be developed by adjusting the location of the loaded stub. In Fig. 10(c), with the decrease of D_9 from 1.3 mm to 1 mm, the loaded stub approaching the zero-voltage point of the third harmonic mode gradually, and the out-of-band suppression is improved from 12.5 dB to 27.3 dB.

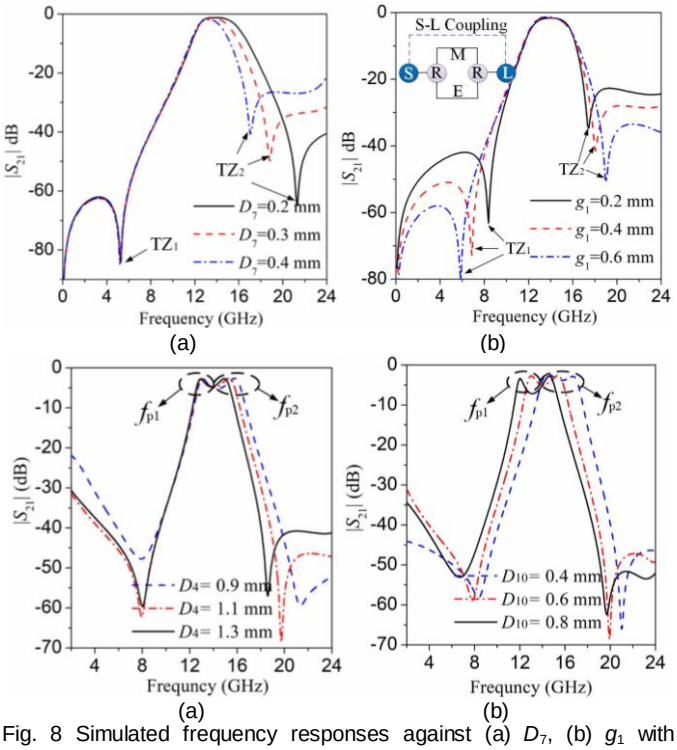

Fig. 8 Simulated frequency responses against (a) D_7, (b) g_1 with coupling topology inserted, (c) D_4 and (d) D_{10}.

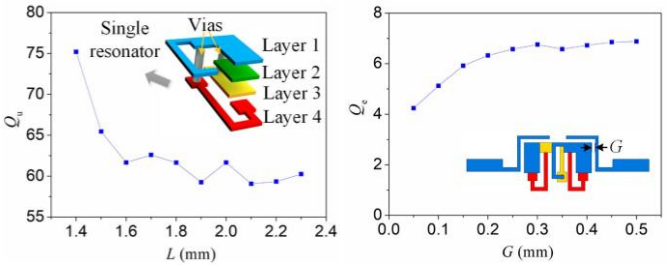

Fig. 9 (a) Simulated Unloaded Q_u of the proposed single resonator against a different L (b) and extracted external quality factors Q_e against a different coupling gap G.

IV. Measurement Result

The performance of the designed BPF is measured from 1 GHz up to 35 GHz. Good agreement between the simulated and measured results is observed in Fig. 11. The dielectric constant of the additive manufactured substrate is 2.75, and the loss tangent is 0.025. [22-23]. The conductivity of the silver film is 3.15×10^6 - 2.52×10^7 σ (S/m) at 20 °C. As demonstrated in Fig. 11, compared with the simulated results achieved by HFSS, the measured insertion loss and return loss are 3.42 dB and 16.65 dB at the center of 12.25 GHz, respectively. In the measurement, the connection between the SMK connector and the filter will cause inter-connection loss, which will lead to a

TABLE I
Comparison with Some Other BPF

Ref.	f_0 (GHz)	*FBW (%)	Number of TZs	Filter order	Stopband (GHz)	$\varepsilon_r/\tan\delta$	Size (mm^2)/ (λ_g^2)	Thickness (mm)/ (λ_g)	Fabricated process
[2]	1.6	22	0	4	0.25 f_0 (20dB)	2.75/0.015	20×83/0.177×0.735	3.6/0.032	Additive manufacturing
	2.45	12	0	4	0.16 f_0 (20dB)	2.35/0.02	11.15×50/0.140×0.626	3.6/0.045	
[11]	33	42.4	0	1	1.58 f_0 (20dB)	N.A.	0.11×0.28/N.A.	N.A.	0.13-μm (Bi)-CMOS
[12]	59.5	21.68	2	2	N.A.	N.A.	0.240×0.225/0.144×0.135	N.A.	0.18-μm CMOS
[24]	4.3	44.2	1	3	2.6 f_0 (20dB)	5.9/N.A.	12×6 /0.418×0.0209	1/0.035	LTCC
This work	12.25	40.8	2	2	1.9 f_0 (20dB)	2.75/0.025	2.7×1.425/0.186×0.098	0.508/0.04	AME solution

*FBW= fractional Bandwidth

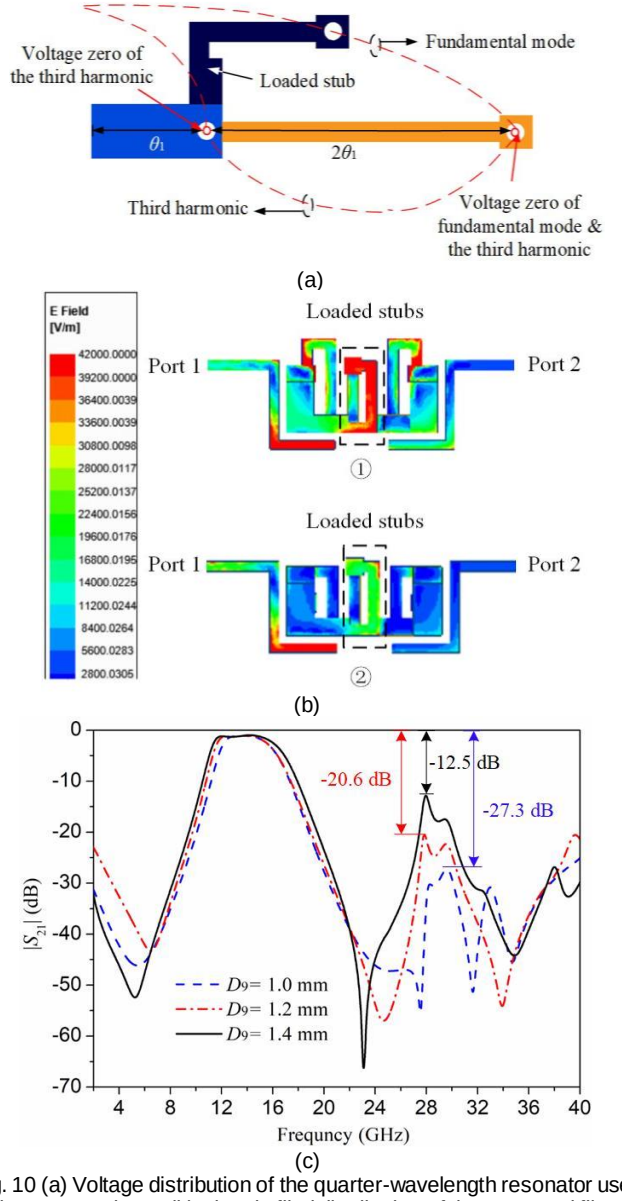

Fig. 10 (a) Voltage distribution of the quarter-wavelength resonator used in the proposed BPF (b) Electric filed distribution of the proposed filter at the resonate frequency of third harmonic mode when ① D_9=1.4mm and ② D_9=1 mm and (c) Simulated $|S_{21}|$ against D_9.

deteriorated insertion loss. At the same time, the error of the thickness in the manufacturing process is also the reason for a deteriorated insertion loss. A 3-dB bandwidth is achieved from 9.58 GHz to 14.57 GHz with the FBW of 40.8%. Two TZs located at 3.51 and 18.51 GHz that can improve the selectivity are generated. In addition, due to the loaded short-circuited stepped impedance stub the upper stopband with more than 20

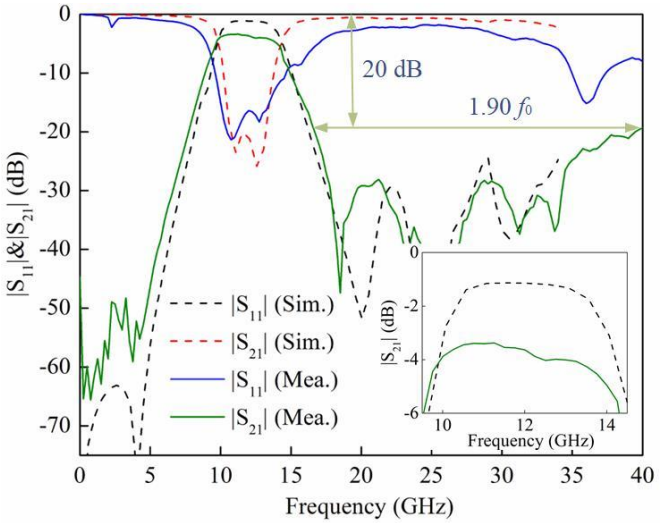

Fig. 11 Simulated and measured frequency response with a zoom-in view of the passband insert loss of the AME printed BPF.

dB rejection level is extended to 23.24 GHz (from 16.65 to 39.89 GHz) or 1.90 f_0. As can be seen, the designed BPF working at 12.25 GHz has the merits of multiple transmission zeros and poles, a compact size, and a wide stopband that can be assigned to television programs or be utilized in radar detection and satellite communications.

Table I shows the comparison of the proposed BPF with other state-of-the-art BPFs fabricated with different fabricated processes. Compared with [2], the BPF proposed in our work has a larger FBW, two flexibly designed transmission zeros, a wider stopband, and a smaller size. In addition, compared with traditional multilayer processes, such as CMOS and LTCC technology, the proposed BPF has a good FBW, high-band and low-band TZs, a good stopband, and a competitive footprint. Furthermore, AME solution used in this paper has the advantages of a low-cost and short processing cycle.

V. Conclusion

In this paper, a low-temperature additively manufactured electronics (AME) technology for multilayer 3D BPF design is presented. Equivalent circuits and Kirchhoff's voltage law are used for analyzing the frequency response of the printed BPF. The proposed additive manufacturing process functions at a typical temperature of 140°C in a standard ambient atmosphere. Good agreement among the calculated, EM simulated and measured results validate the feasibility of the proposed AME solution for miniaturized bandpass filter design. The proposed AME solution has great potential in circuit-in-package applications.

REFERENCES

[1] F. Cai, Y. Chang, K. Wang, C. Zhang, B. Wang and J. Papapolymerou, "Low-loss 3-D multilayer transmission lines and interconnects fabricated by additive manufacturing technologies," *IEEE Trans. Microw. Theory Techn.*, vol. 64, no. 10, pp. 3208–3216, Oct. 2016, doi: 10.1109/TMTT.2016.2601907.

[2] A. Vallecchi, D. Cadman, W. G. Whittow, J. Vardaxoglou, E. Shamonina and C. J. Stevens, "3-D printed bandpass filters with coupled vertically extruded split ring resonators," *IEEE Trans. Microw. Theory Techn.*, vol. 67, no. 11, pp. 4341-4352, Nov. 2019, doi: 10.1109/TMTT.2019.2934456.

[3] Y. Gu, D. Park, S. Gonya, J. Jendrisak, S. Das and D. R. Hines, "Direct-write printed broadband inductors," *Addit. Manuf.*, vol. 30, 100843, Dec. 2019, doi: 10.1016/j.addma.2019.100843.

[4] P.F. Flowers, C. Reyes, S. Ye, M. J. Kim and B. J. Wiley, "3D printing electronic components and circuits with conductive thermoplastic filament," *Addit. Manuf.*, vol. 18, pp. 156-163, Dec. 2017, doi: 10.1016/j.addma.2017.10.002.

[5] P. Pa, Z. Larimore, P. Parsons and M. Mirotznik, "Multi-material additive manufacturing of embedded low-profile antennas," *Electron. Lett.*, vol. 51, no. 20, pp. 1561-1562, 2015, doi: 10.1049/el.2015.2186.

[6] J. Zhu, Y. Yang, S. Li, S. Liao and Q. Xue, "Single-ended-fed high-gain LTCC planar aperture antenna for 60 GHz antenna-in-package applications," *IEEE Trans. Ant. and Propag.*, vol. 67, no. 8, pp. 5154-5162, Aug. 2019, doi: 10.1109/TAP.2019.2917591.

[7] Z. Chen, Y. P. Zhang, A. Bisognin, D. Titz, F. Ferrero and C. Luxey, "A 94-GHz dual-polarized microstrip mesh array antenna in LTCC technology," *IEEE Antennas Wirel. Propag. Lett.*, vol. 15, pp. 634-637, 2016, doi: 10.1109/LAWP.2015.2465842.

[8] J. Xu and X. Y. Zhang, "Compact high-isolation LTCC diplexer using common stub-loaded resonator with controllable frequencies and bandwidths," *IEEE Trans. Microw. Theory Techn.*, vol. 65, no. 11, pp. 4636-4644, Nov. 2017, doi: 10.1109/TMTT.2017.2697855.

[9] X. Dai, X. Y. Zhang, H. Kao, B. Wei, J. Xu and X. Li, "LTCC bandpass filter with wide stopband based on electric and magnetic coupling cancellation," *IEEE Trans. Compon. Packag. Manuf. Technol*, vol. 4, no. 10, pp. 1705-1713, Oct. 2014, doi: 10.1109/TCPMT.2014.2346240.

[10] B. Zhang, D. Titz, F. Ferrero, C. Luxey and Y. P. Zhang, "Integration of quadruple linearly-polarized microstrip grid array antennas for 60-GHz antenna-in-package applications," IEEE *Trans. Compon. Packag. Manuf. Technol.*, vol. 3, no. 8, pp. 1293-1300, Aug. 2013, doi: 10.1109/TCPMT.2013.2255333.

[11] Y. Yang, H. Liu, Z. J. Hou, X. Zhu, E. Dutkiewicz and Q. Xue, "Compact on-chip bandpass filter with improved in-band flatness and stopband attenuation in 0.13-μm (Bi)-CMOS technology*," IEEE Electron.Device Lett.*, vol. 38, no. 10, pp. 1359-1362, Oct. 2017, doi: 10.1109/LED.2017.2739186.

[12] A. S. El-Hameed, A. Barakat, A. B. Abdel-Rahman, A. Allam, and R. K. Pokharel, "Ultracompact 60-GHz CMOS BPF employing broadside-coupled open-loop resonators," *IEEE Microw. Wireless Compon. Lett.*, vol. 27, no. 9, pp. 818–820, Sep. 2017, doi: 10.1109/LMWC.2017.2734771.

[13] M. Li, Y. Yang, K. D. Xu, X. Zhu and S. W. Wong, "Microwave on-chip bandpass filter based on hybrid coupling technique," *IEEE Trans. Electron Devices*, vol. 65, no. 12, pp. 5453-5459, Dec. 2018, doi: 10.1109/LMWC.2017.2734771.

[14] V. F. Tseng and H. Xie, "Increased multilayer fabrication and RF characterization of a high-density stacked MIM capacitor based on elective etching," *IEEE Trans. Electron Devices*, vol. 61, no. 7, pp. 2302-2308, July 2014, doi: 10.1109/TED.2014.2325491.

[15] Y. Li, L. Ge, J. Wang, B. Ai, M. Chen, Z. Zhang, Z. Li, "A Ka-band 3-D-printed wideband stepped waveguide-fed magnetoelectric dipole antenna array," *IEEE Trans. Antennas Propag.*, vol. 68, no. 4, pp. 2724-2735, April 2020 , doi: 10.1109/TAP.2019.2950868.

[16] G. Wu, Y. Zeng, K. F. Chan, S. Qu and C. H. Chan, "3-D printed circularly polarized modified fresnel lens operating at terahertz *frequencies*," *IEEE Trans. Antennas Propag.*, vol. 67, no. 7, pp. 4429-4437, July 2019, doi: 10.1109/TAP.2019.2908110.

[17] M. Laurila, B. Khorramdel and M. Mäntysalo, "Combination of e-jet and inkjet printing for additive fabrication of multilayer high-density RDL of silicon interposer," *IEEE Trans.* Electron *Devices.*, vol. 64, no. 3, pp. 1217-1224, March 2017, doi: 10.1109/TED.2016.2644728.

[18] G. Huang, C. Han, W. Xu, T. Yuan and X. Zhang., "A compact 16-way high-power combiner implemented via 3-D metal printing technique for advanced radio-frequency electronics system applications" *IEEE Trans. Ind. Electron.*, vol. 66, no. 6, pp. 4767-4776, June 2019, doi: 10.1109/TIE.2018.2863219.

[19] S. Kyung, J. Kwon, Y. Kim and S. Jung, "Low-temperature, solution-processed, 3-D complementary organic FETs on flexible substrate," in *IEEE* Trans. *Electron Devices*, vol. 64, no. 5, pp. 1955-1959, May 2017, doi: 10.1109/TED.2017.2659741.

[20] P. Rewatkar and S. Goel, "Next-generation 3D printed microfluidic membraneless enzymatic biofuel cell: cost-effective and rapid approach," *IEEE Trans. Electron Devices.*, vol. 66, no. 8, pp. 3628-3635, Aug. 2019 , doi: 10.1109/TED.2019.2922424.

[21] Y. Sakabe, M. Hayashi, T. Ozaki and J. P. Canner, "High frequency performance of multilayer ceramic capacitors," *1995 Proceedings. 45th Electronic Components and Technology Conference*, Las Vegas, NV, USA, 1995, pp. 234-240, doi: 10.1109/ECTC.1995.514390.

[22] M. Li, Y. *Yang*, F. Iacopi, J. Nulman and S. Chappel-Ram, "3D-printed low-profile single-substrate multi-metal layer antennas and array with bandwidth enhancement," *IEEE Access*, vol. 8, pp. 217370-217379, 2020. doi: 10.1109/ACCESS.2020.3041232.

[23] M. Li, Y. Yang, Y. Zhang, F. Iacopi, S. Ram, J. Nulman, "A fully integrated conductive and dielectric additive manufacturing technology for microwave circuits and antennas," *the 50th European Microwave Conference (EuMC)*, accepted, 2020.

[24] X. J. Zhang, H. H Zhang and X. P. Ma, "Design of compact wideband LTCC filter using pentagonal-shaped SIR," *Electron. Lett*., vol. 47, no. 5, pp. 327–329, 2011, doi:10.1049/el.2012.4071

MENGZE LI (Student Member, IEEE) was born in Hunan, China, in 1994. She received the B.Eng. degree in electrical engineering and automation from Hunan University, Hunan, in 2015, and the M.Eng. degree in electronic field and microwave technology from Xiamen University, Xiamen, China, in 2018. She is currently pursuing the Ph.D. degree with the Faculty of Engineering and Information Technology, University of Technology Sydney, Australia. From 2017 to 2018, she was a Visiting Student with the Faculty of Engineering and Information Technology, University of Technology Sydney.

Her current research interests include microstrip filters, multiplexers, RFIC, reflectarrays and 3-D print technology.

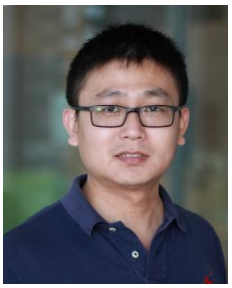

Dr. Yang Yang (S'11–M'14-SM'17) was born in Bayan Nur and grew up in Hohhot, Inner Mongolia, China. He received the MEng, MSc, and PhD degrees from Department of Electrical and Computer Systems Engineering (ECSE) in Clayton Campus, Monash University, Melbourne, Australia, in 2007, 2008 and 2013, respectively.

Dr. Yang has three years industry experience at Rain Bird Australia serving as an Asia Pacific GSP Engineer, during 2012 to 2015. He received the corporate 2014 Global GSP Success Award (one globally). In April 2015, he returned to academia and served as a Senior Research Associate with the Centre for Collaboration in Electromagnetic and Antenna Engineering at Macquarie University. In April 2016, he was appointed as a Research Fellow with State Key Laboratory of Terahertz and Millimeter Waves, City University of Hong Kong. Since December 2016, Dr. Yang joined University of Technology Sydney, Australia. He is currently a Senior Lecturer and a team leader of Millimetre-Wave Integrated Circuits and Antennas. His research interests include millimetre-wave and sub-terahertz technologies in 5G and biomedical applications. He has over 170

international peer reviewed publications in microwave, millimetre-wave and terahertz circuits and antennas.

Professor Francesca Iacopi (IEEE Senior Member) has over 20 years' international industrial and academic expertise in the miniaturisation of semiconductor technologies. She has led large R&D projects for IMEC (Belgium) and Globalfoundries Inc (USA) in interconnects, electronic devices and packaging. Her focus is the translation of basic scientific advances into nanomaterials and device concepts into integrated technologies. She is known for her work in porous dielectrics for interconnects, and, more recently, graphene for on-chip applications. She is a recipient of an MRS Gold Graduate Student Award (2003), an ARC Future Fellowship (2012), and a Global Innovation Award in Washington DC (2014), she was listed among the most innovative engineers by Engineers Australia (2018). Francesca is a Fellow of the Institution of Engineers Australia and currently serves in several technical committees for the Materials Research Society, the IEEE Electron Devices Society, as well as the International Roadmap for Systems and Devices. She leads the Integrated Nanosystems Lab, in the Faculty of Engineering and IT, University of Technology Sydney and is a Chief Investigator of the ARC Centre of Excellence in Transformative Meta-Optical Systems.

Minoru Yamada was born in Toyama, Japan, in 1952. He was involved the Electronics product development more than 40 years especially wireless telecommunication products such as voice and video data transfer system using DECT technology. He was developed more than 50 products and sold in market under British telecom, Motorola, Philips, Uniden, Telstra and some others brands. His responsibility was mainly RF hardware and software development. Last 20 years were mainly managing the R&D department and product architecture development.

Dr. Jaim Nulman (IEEE Senior Member) received an undergraduate degree from Technion-Israel Institute of Technology, a graduate degree and a doctorate from Cornell University, all in Electrical Engineering, and an MBA from Stanford University. He is a proven influencer and innovator with more than 30 years of expertise in working with companies from start-ups to Fortune 500 enterprises. He served as Vice President of Applied Materials, where he spent 15 years in several product division and corporate positions. He drove the successful commercialization of one of Applied Materials' semiconductor manufacturing products with impressive market penetration of $1 billion in less than five years. He is a co-inventor in over 30 patents in the area of semiconductor manufacturing technology, semiconductor manufacturing equipment, and additive manufacturing for electronics. He has served as invited lecturer at UC Berkeley extension, and NATO's International Summer Institute.